

# Internal motion of soft granular particles under circular shearing: Rate-dependent quaking and its spatial structure

Jr-Jiun Lin <sup>(1,2,\*)</sup>, Cheng-En Tsai <sup>(3,1)</sup>, Jung-Ren Huang<sup>(1)</sup>, and Jih-Chiang Tsai <sup>(1,\*)</sup>

<sup>1)</sup> Institute of Physics, Academia Sinica, Taipei, Taiwan

<sup>2)</sup> Physics Department, National Tsing Hua University, Hsin-Chu, Taiwan

<sup>3)</sup> Physics Department, National Taiwan University, Taipei, Taiwan

Correspondence (\*): Jr-Jiun Lin <linjrjun@gmail.com>, JC Tsai <jctsai@phys.sinica.edu.tw>

Tightly packed granular particles under shear often exhibit intriguing intermittencies, specifically, sudden stress drops that we refer to as quaking. To probe the nature of this phenomenon, we prototype a circular shear cell that is capable of imposing a uniform and unlimited shear strain under quasi-static cyclic driving. Spherical PDMS (polydimethylsiloxane) particles, immersed in fluid, are driven in a fixed total volume at a wide range of shear rates, with particle trajectories captured in 3D space via refraction-index-matched fluorescent tomography. Statistics on the magnitude of fluctuating displacements of individual particles shows distinct dependence on the shear rate. Particles move smoothly at high shear rates. At intermediate shear rates, quaking emerges with clusters of particles exhibiting relatively large displacements. At low shear rates, a cluster can span the entire system and the cluster exhibits substructures in view of localized particle movements. Overall, we have confirmed that the quaking phenomena in the current setup are consistent with our previous work [*Phys. Rev. Lett.*, 126, 128001 (2021)], and that the dimensionless shear rate that we have proposed is indeed a good parameter for unifying the transitions observed in different experimental geometries.

## I. INTRODUCTION

Granular material exhibits multifaceted flow properties that are ubiquitous in nature, such as those directly related to geological phenomena ranging from surface creep [1–3] to earthquakes [4–6]. Such wide variety has motivated various physical descriptions under different conditions. In particular, there are two prevailing categories: visco-plastic models [7–10] and those derived from dense suspensions [11]. The former describes the regime dominated by interparticle contacts, in which the strain concentrates in highly localized plastic regions known as shear transformation zones [9,12,13]. Meanwhile, the latter invokes the viscous number and shear thickening behaviors [14–16] to capture scenarios where the interstitial fluid becomes dynamically relevant via lubrication and viscous force.

In an effort to bridge the two narratives, our previous experimental study [17] presents a continuous transition from “granular solid” to “granular fluid” that depends explicitly on shear rate. The onset of this solid-fluid transition is distinctly marked by the occurrence of intermittent stress release, that are often referred to as “avalanche” or “quake” in the literature [18–21]. Such intermittency is asserted to stem from the speed dependence of inter-particle friction, a general tribological property vindicated by measurements [22,23]. In a further numerical study [24], we have shown that adding the speed dependence of interparticle friction is sufficient in generating the empirically observed quaking behaviors reported in Ref.[17]. The behaviors are well described by a dimensionless shear rate  $S_\ell \equiv \ell\dot{\gamma}/V_c$ , in which  $\ell$  stands for particles size,  $\dot{\gamma}$  the physical shear rate, and  $V_c$  the material-specific speed beyond which the friction drops substantially. While  $S_\ell \gg 1$  and  $S_\ell \ll 1$  stands for the scenarios with full lubrication and conventional Coulomb friction between particles, respectively, quaking prevails in granular flows with intermediate values of  $S_\ell$  [24].

The grain-scale dynamics of granular flow has been widely explored via various experimental techniques. Previous works implement quasi-2D systems [4,21,25] that unveils individual grain motion as well as force chain structures. Meanwhile, 3D bulk imaging techniques, such as refraction index matched imaging [19,26,27], x-ray tomography [28–30], and magnetic resonance imaging [31,32] have been developed to capture the internal structure of granular media. These technologies enabled delicate 3D experiments that shed light on local response to shear before macroscopic yielding, such as the overall spatio-temporal correlation of local strain [19] and the network topological evolution [29,30].

In the present study, we take advantage of a fast 3D scanning scheme and capture the grain-scale kinematics of individual quaking events through a wide range of shear rates, all under the regime of low-inertia steady flow. We present the real-time 3D spatial structure of quaking events and its shear rate dependence, expanding the scope of our previous analysis [17] which mainly focus on the transition of stress patterns and its implications.

## II. SETUP AND OVERVIEW OF THE RATE-DEPENDENT TRANSITION

We have established a prototype of Circular Shear Cell (CSC), which is shown in Fig.1: The sidewall of the cell is formed by a stack of acrylic rings that are driven cyclically by four steel rods going through the rings. The four rods are rotating in phase, with their lower ends fixed at the base plate with a rotary joint. The orientation of these rods specifies an unit vector  $\hat{s}$  that rotates at an adjustable angular speed  $\Omega$  and defines three orthogonal unit vectors  $\{\hat{s}, \hat{\phi}, \hat{z}\}$  at every instant as shown on the graph. In the laboratory frame of reference, the driving imposes a base flow  $\vec{v}^0(\vec{x}, t) = \Omega (z - z_0) \tan \alpha \hat{\phi}$  in which  $z_0$  stands for the height of the base plate and, at every instant, the flow field exhibits a spatial gradient that has a component  $\frac{\partial v_{\phi}^0}{\partial z} \equiv \dot{\gamma}_{inst} = \Omega \tan \alpha$  while all other components are zero. The constant  $\dot{\gamma}_{inst}$  can be regarded as an effective shear rate on the  $\phi z$ -plane. By design, we set the angle  $\alpha$  to be sufficiently large ( $\tan \alpha = 0.45$ ) so that the particles are incrementally rearranged and never come back to the same positions after one complete cycle of driving, as validated by particles trajectories detailed in Supplemental Materials. (The effective shear strain for one complete driving cycle is  $\gamma_0 \equiv \int \dot{\gamma}_{inst} dt = \int \Omega \tan \alpha dt = 2\pi \tan \alpha \approx 2.8$ .)

The cell is packed at a fixed volume fraction = 0.59 with a binary mixture of molded PDMS (polydimethylsiloxane) spheres (Young's modulus  $\approx 1.5$  MPa) having diameters 9 and 12  $\mu\text{m}$ , respectively mixed at the number ratio 3:2. The CSC setup has a diameter  $2R_{total} = 35$  cm and height  $H_{total} = 10$  cm, which forms a bulk of  $\approx 10^4$  particles. The interstitial space is filled with glycerol-water mixture that index-matches the particles containing LASER-activated fluorescent dye (Rhodamine B). Using a rotating cube, we are able to shift a horizontal LASER sheet (supplied by COHERENT Verdi G5, at 532nm) periodically by a distance up to 6 cm in the  $z$  direction, at rates ranging from 10 to 0.008 Hz. Time-resolved tomographic images are captured via a high-speed camera (PHANTOM VEO) underneath. A sample image is shown in Fig. 2. Note that the two types of particles are dyed differently, allowing us to easily distinguish them in tomographic images. Due to multiple scattering, the LASER sheet disperses, resulting blurred images at the farther half of the imaging area. Therefore we adopt only half of the image that is closer to the LASER source for analyses --- see the boxed region in Fig. 2. The 3D image stack is formed by a series of 100 images captured over a complete scan. In our analyses, we consider a stack corresponding to a  $12\text{cm} \times 20\text{cm} \times 6\text{cm}$  space containing roughly 1200 particles that are far from the boundary. The 3D trajectories of these particles can be obtained via TRACKPY [33,34]. The details of 3D image reconstruction and particle tracking can be found in Supplemental Materials.

The base plate is constrained by four surrounding force sensors placed at an offset distance  $r_{off}$  away from the central axis, as shown by the topview in Fig. 1. This configuration allows us to determine both the net force  $\vec{f}_{xy}$  and the torque exerted on the base plate ---see Supplemental Materials.

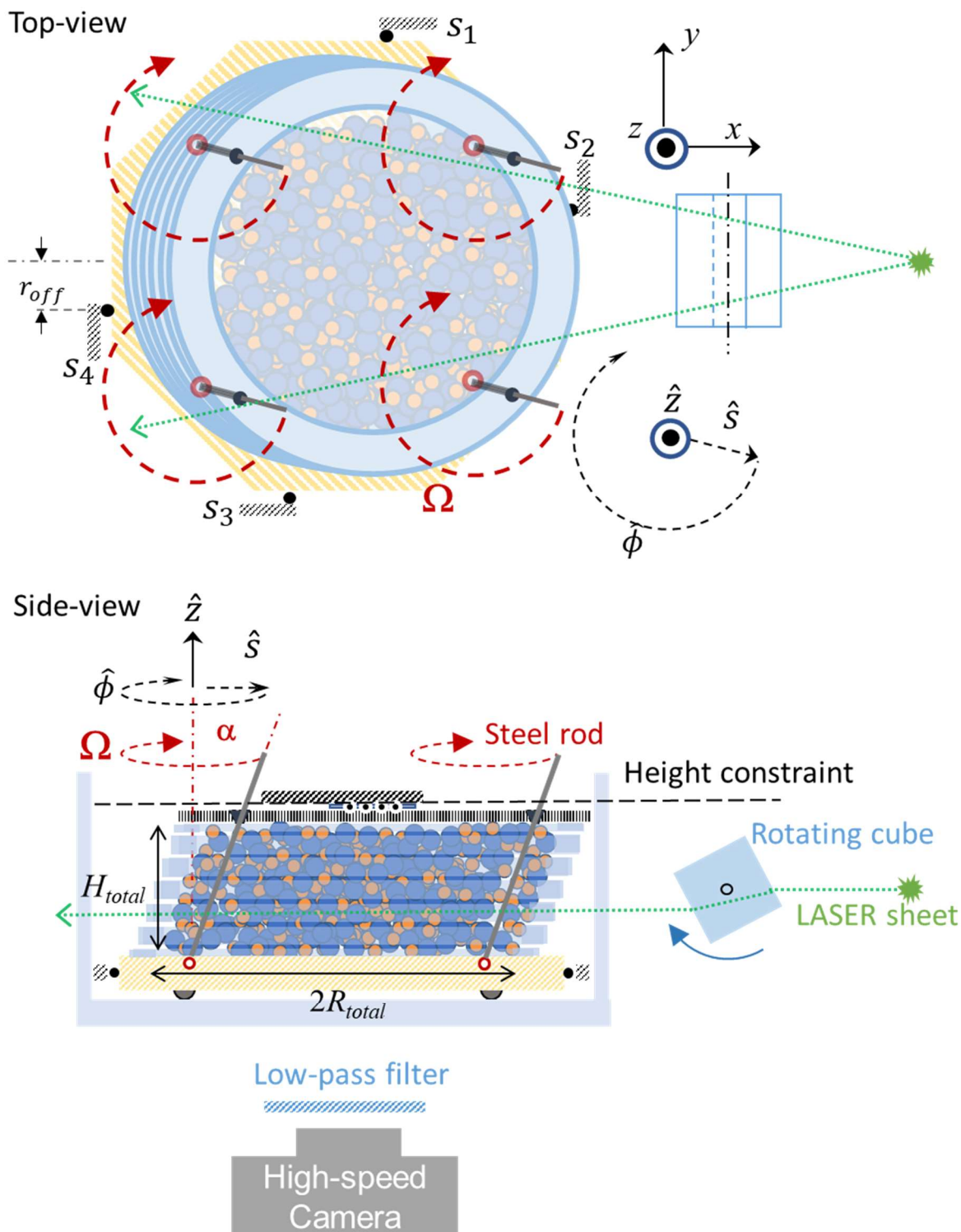


**FIG.1** Schematics of the device: The topview highlights that the four steel rods (and in turn the acrylic rings) are doing circular motions sharing the same angular speed  $\Omega$ . At every instant, the orientation of the rods defines the unit vectors  $\hat{s}$  and  $\hat{\phi}$ . The four force sensors that keep the octagonal base plate (yellow shaded) in place are labelled as  $S_1 \sim S_4$ . The sideview shows that the rotating cube creates a periodic vertical scan by the LASER sheet that penetrates the granular packing, whose total volume is constrained from the top.

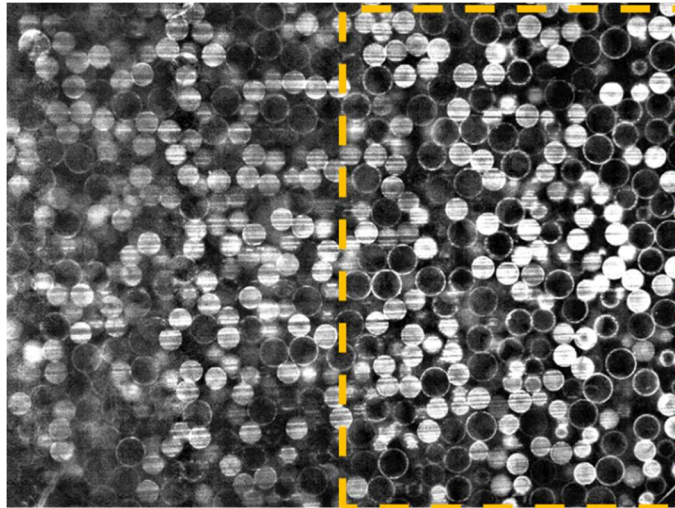


**FIG.2** –Typical tomographic image. The 9 mm particles appear as white disks and the 12 mm particles as hollow circles. The yellow dashed box shows the half of the image used in our analyses.

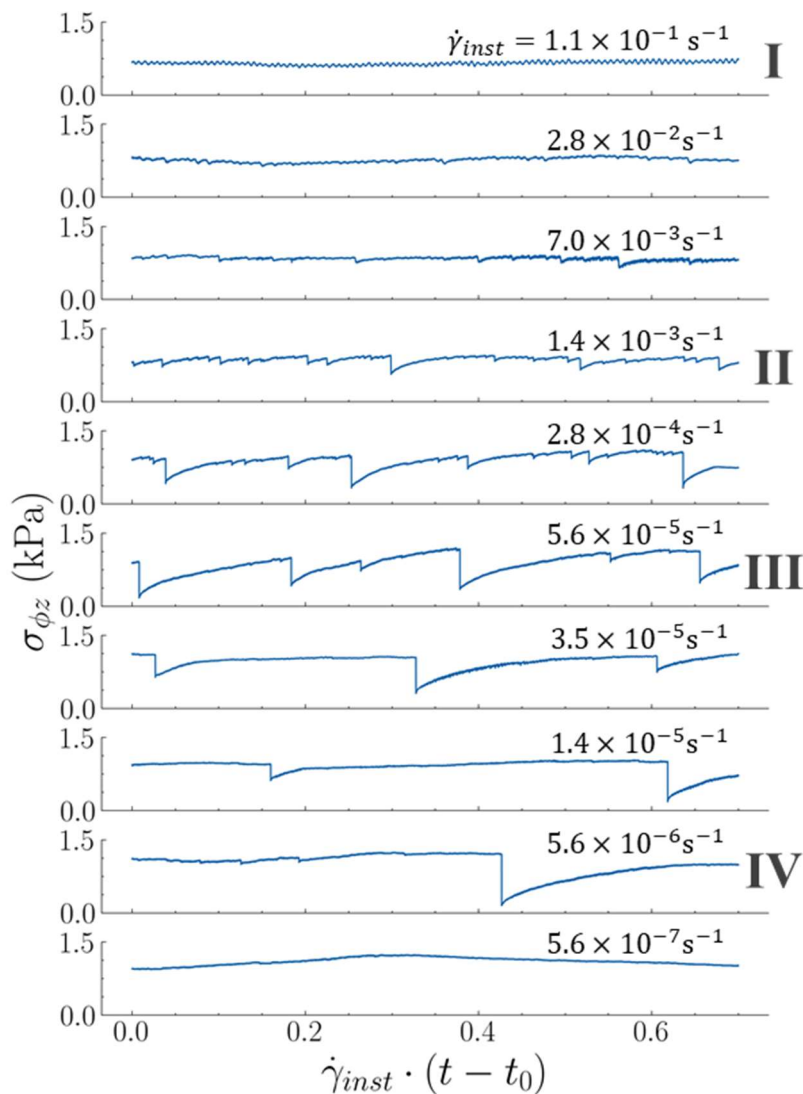


**FIG.3** Time sequence of the instantaneous shear stress  $\sigma_{\phi z}$  for various values of shear rate (marked at upper-right corner of every sub-plot). Roman numerals mark the four signature cases that will be referred to in the upcoming sections. For each run, we start the motor at  $t = 0$ , and all recordings begin at  $t = t_0$  such that  $\Omega t_0 = 0.5\pi$ . This provides a preshear  $\approx 0.7$  to ensure that the system has reached a steady state for each intended shear rate.

Force signals in Fig.3 provide an overview of the gradual transition over the change of the shear rate  $\dot{\gamma}_{inst}$ . Our typical sampling rate is 1000 Hz. The force that opposes the shear strain is  $f_{\phi} \equiv \overline{f_{xy}} \cdot (-\hat{\phi})$ . The instantaneous shear stress  $\sigma_{\phi z}$ , is determined as  $f_{\phi}$  divided by the cross-sectional area of the cell (961cm<sup>2</sup>). In obtaining  $f_{\phi}$ , we have also removed the contribution from a mechanical artifact (around 10% of the mean value) --- please see Supplemental Materials for its detail. Fig. 3 compares the time sequences of shear stress  $\sigma_{\phi z}$  at a wide range of driving rates. At high shear rates,  $\sigma_{\phi z}$  is smooth with merely negligible high-frequency oscillations. As  $\dot{\gamma}_{inst}$  decreases, the time sequence of shear stress displays increasingly larger sudden drops, which we refer to as “quakes”. At  $\dot{\gamma}_{inst} = 5.6 \times 10^{-5} \text{ s}^{-1}$ , the drops reach magnitudes that are comparable to the mean value. Interestingly, as  $\dot{\gamma}_{inst}$  decreases below  $5.6 \times 10^{-5} \text{ s}^{-1}$ , substantial quakes get separated by increasingly larger strain. For the run with the slowest rate ( $5.6 \times 10^{-7} \text{ s}^{-1}$ ), we do not find any significant quakes in our observation time window (of roughly two weeks, with an effective strain  $\approx 0.7$ ). The time sequences of  $\sigma_{\phi z}$  thus provide a good overview of the transition over shear rates ranging over six order of magnitudes. For the convenience of further discussion, we use roman numerals I~IV in Fig. 3 to indicate four signature cases that will be the focus of further analyses.

### III. MAIN RESULTS

We calculate the displacement  $\Delta\vec{r}$  of each grain over one strain step  $\Delta\gamma = \dot{\gamma}_{inst} \delta t$ , which is set to be  $\gamma_0/800 \approx 3.5 \times 10^{-3}$  for all runs except for two exceptions<sup>1</sup>. A generic snapshot of  $\Delta\vec{r}$  vectors at an quiescent interval is shown in Fig. 4(a), which is 3D rendered via OVITO [35,36]. Particle movements are primarily in the  $\hat{\phi}$  direction and dictated by the base flow  $\vec{v}^0(\vec{x}, t)$  imposed by the driving mechanism, as is evident by the vertical gradient of these vectors. (Note that  $\vec{v}^0$  is strictly in the  $\phi z$ -plane at every instant, with its magnitude linearly proportional to the height above the base plate.) In contrast, Fig.4(b) displays the sudden ‘‘jumps’’ of particles upon a quaking event, showing extraordinarily large displacements in apparently random directions.

In further analyses shown in the upcoming subsections, we have removed the contribution from the base flow, by defining the *fluctuating displacement*  $\delta\vec{r}$  for each particle, specifically, as

$$\delta\vec{r} = \vec{r}(t) - \vec{r}(t - \delta t) - \vec{v}^0(\vec{r}, t)\delta t$$

where  $\vec{r}(t)$  is the particle position at time  $t$ .

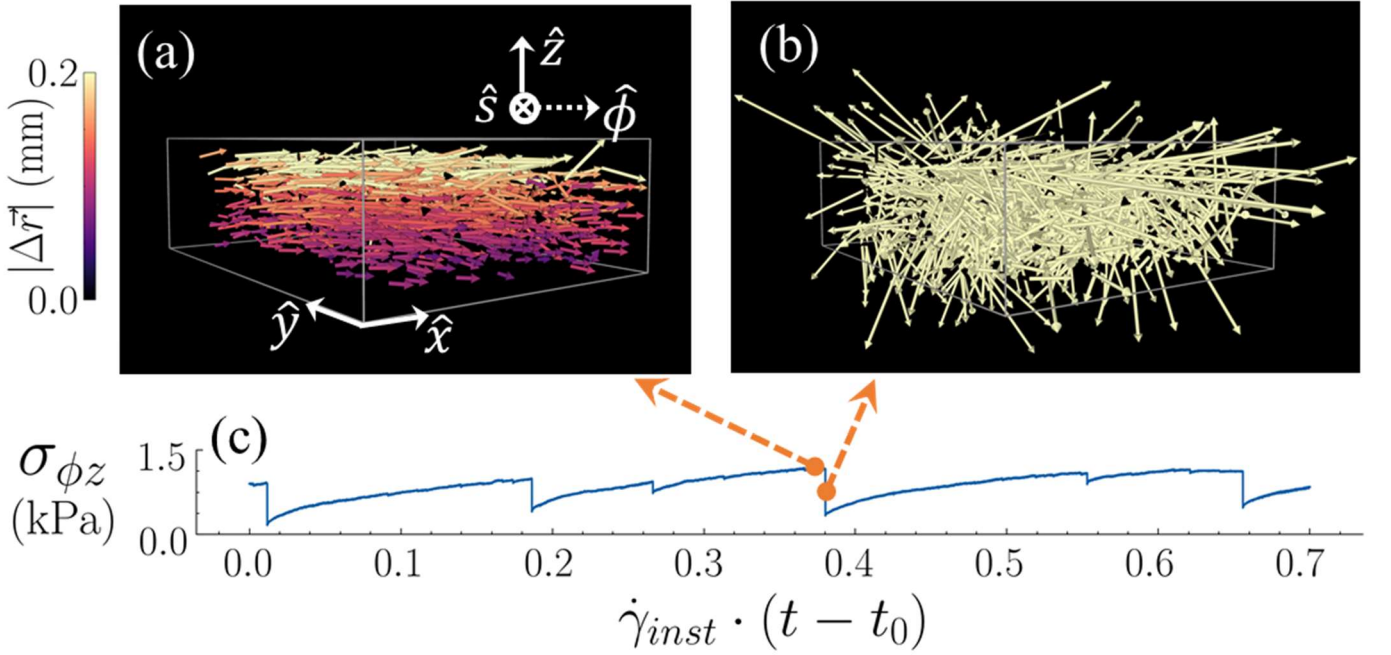


**FIG.4** – 3D reconstructed displacements associated with two adjacent time intervals in case III, as are viewed from the  $\hat{s}$  direction perpendicular to the  $\phi z$ -plane: **(a)** a quiescent interval immediately before a quaking event, showing the contribution from the base flow. **(b)** an interval in which a quaking occurs. **(c)** The time sequence of the instantaneous shear stress. The two intervals associated with (a) and (b) share the same effective strain step  $\Delta\gamma = 3.5 \times 10^{-3}$  and the same color bar for the magnitude of displacement. For visibility, the displacement vectors in (a) and (b) are exaggerated by a factor of 100 and 20, respectively.

<sup>1</sup> Due to limited laser power and fluorescence, camera frame rate could not exceed 1000/s for a properly illuminated image. Under this constraint, case I (with  $\dot{\gamma}_{inst} = 1.1 \times 10^{-1} \text{ s}^{-1}$ ) is scanned at strain intervals of  $16\Delta\gamma$ , while the case with  $\dot{\gamma}_{inst} = 2.8 \times 10^{-2} \text{ s}^{-1}$  at  $4\Delta\gamma$ .

### A. Fluctuation over time

The rate-dependent quaking transition, outlined by the force measurements in the previous section, can now be characterized from the perspective of grain displacements. In Fig.5(a), each curve represents the cumulative distribution function of  $|\delta\vec{r}|$  of all particles for one time interval. For each case, data of all time intervals are plotted. The spreading of the curves thus represents the time fluctuation of  $|\delta\vec{r}|$  distribution for the granular system. The horizontal axis is scaled by the all-time average of each case  $\langle|\delta\vec{r}|\rangle$ .

In case I, the spread of the curves is relatively narrow, as the grain flow is smooth and homogeneous in time. The spread of the curves over time widens as the shear rate  $\dot{\gamma}_{inst}$  decreases. In case II, the medians of  $|\delta\vec{r}|/\langle|\delta\vec{r}|\rangle$  at different times spread throughout a range wider than one order of magnitude, whereas in case III a handful of distinct curves stand out from the majority. These curves reveals the individual quaking moments when a significant fraction of  $|\delta\vec{r}|$  values jumps above  $\langle|\delta\vec{r}|\rangle$ , while the majority of curves that aggregate on the left correspond to the quiescent moments.

To quantify the spread of the curves, we calculate the time variation of the medians on logarithmic scale,  $\Sigma$ , and plot it in Fig. 5(b) as a function of  $\dot{\gamma}_{inst}$ . The plot shows an intriguing non-monotonic behavior with a peak at case III: As the value of  $\dot{\gamma}_{inst}$  decreases toward that of case IV, even though the extreme case exhibits a huge deviation from the main cluster of curves, its occurrence corresponds to only a single quaking event (as shown in Fig.3). The decrease in  $\Sigma$  with  $\dot{\gamma}_{inst}$  (from III to IV) results from the rareness of large quakes at very small shear rates.

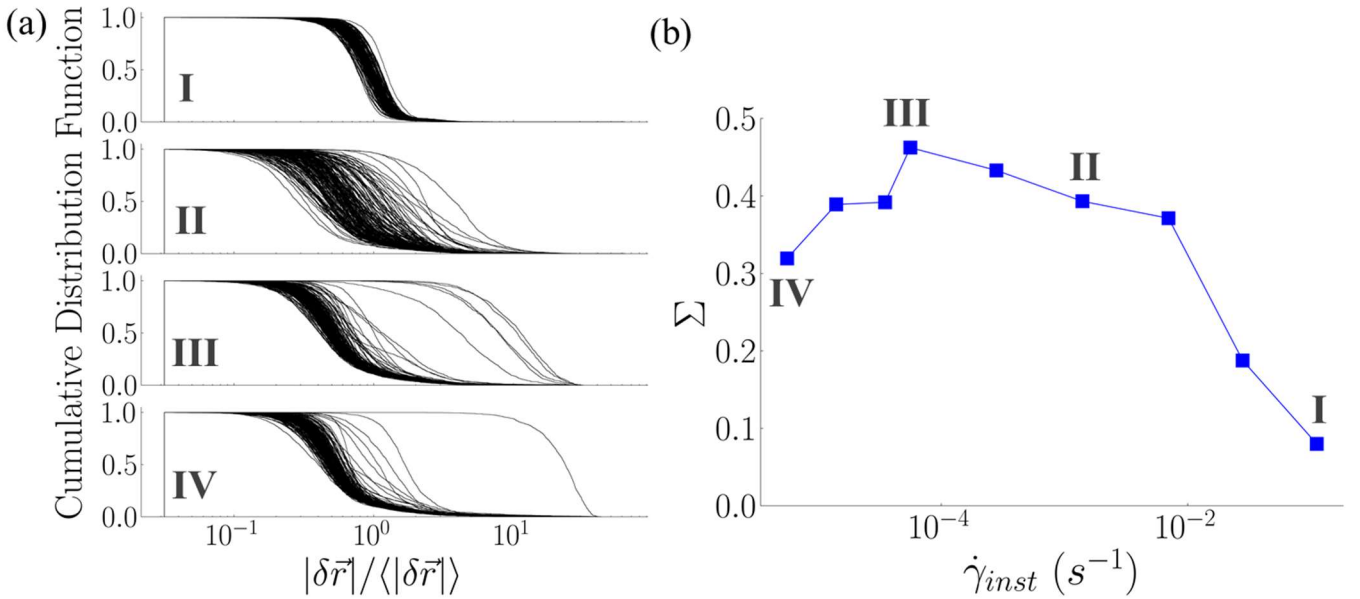


**FIG.5** Statistics based on snapshots of  $|\delta\vec{r}|$ . **(a)** Cumulative distribution function showing the fraction of particles that has its  $|\delta\vec{r}|/\langle|\delta\vec{r}|\rangle$  above the value specified on the horizontal axis, where  $\langle|\delta\vec{r}|\rangle$  stands for the average over all particles and all time for each run. **(b)** The logarithmic spread,  $\Sigma$ , as defined in the main text, as a function of the shear rate  $\dot{\gamma}_{inst}$ . The roman numerals indicate the four signature cases defined in Fig.3.



## B. Clusters of large displacements

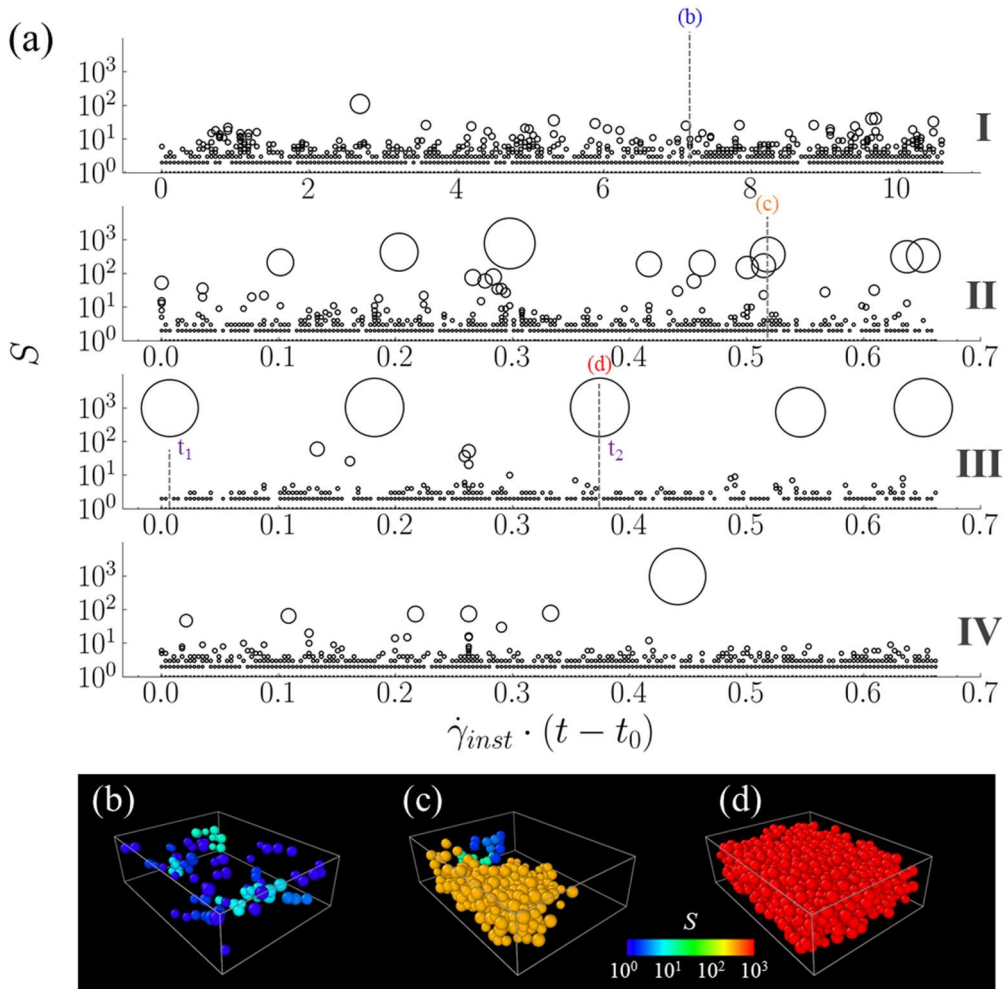
We proceed to show explicitly how the rearrangements are clustered in space using a simple clustering approach. First, we find the nearest neighbors for each particle by applying Laguerre tessellation [37], which accounts for the different radii of the two types of particle. We then consider only the *significantly rearranged* particles with values of  $|\delta\vec{r}|$  ranking in the top 5% in each case. (The results we obtain in this subsection are qualitatively similar for different choices of this percentile threshold -- see Supplemental Materials.) A group of significantly rearranged particles that can be interconnected via Laguerre bonds is defined as one cluster. Following such definition, all significantly rearranged particles can be grouped into clusters. We define the clusters size  $S$  to be the number of particles in each cluster.

To understand whether these significantly rearranged particles are sparsely dispersed or tightly clustered, we plot in Fig.6(a) the occurrence of clusters of various sizes as a time sequence for each of the signature case, in which every cluster is presented with a circle that is proportional to its size  $S$ . Note that the total number of particles participating the plot is approximately the same for all four cases, because experimentally the total number of tracked particles is roughly fixed.

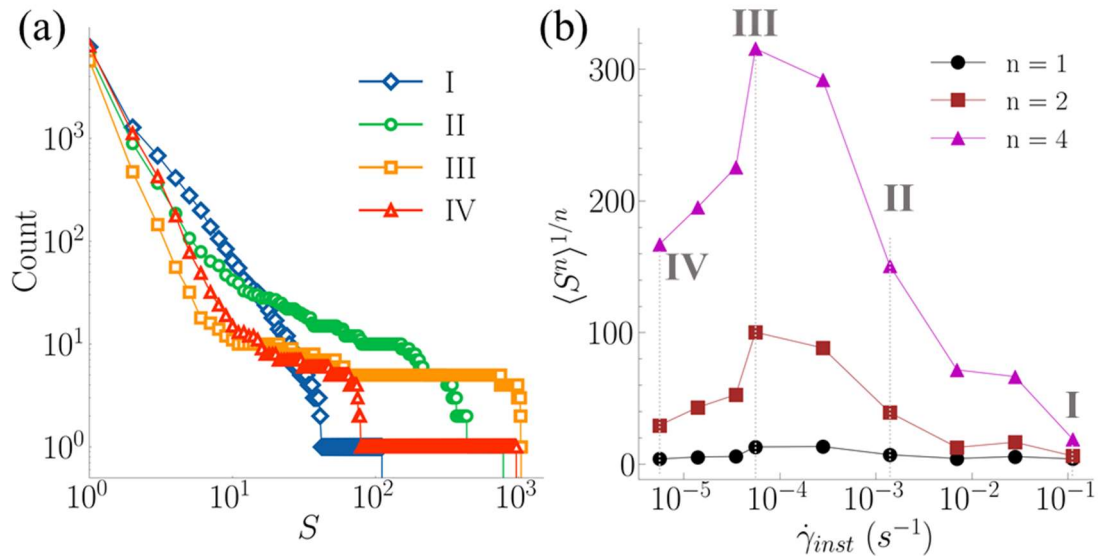
At the fastest shear rate (case I), the values of  $S$  rarely surpass 10, while clusters are scattered evenly in space and time, as illustrated in Fig. 6(b). In case II, large clusters with sizes up to several hundred emerge, which can occupy a considerable fraction of the whole volume. Interestingly, relatively large clusters in this case are often accompanied by numerous small clusters. This is visually demonstrated in the snapshot in Fig. 6(c). In case III, a handful large clusters with  $S \sim 1000$  virtually spans the entire trackable region, as shown in Fig. 6(d). These system-spanning quakes correspond to the outstanding curves in Fig. 5(a). In case IV, only one major quake remains.

Fig. 7(a) shows the all-time cumulative distributions of  $S$  for each of the four cases. The results summarize the change of behaviors in a quantitative manner. We find that, from case I to III, the distribution develops a long tail that reaches size  $\sim 1000$  and saturates the system, resulting in an apparent sharp cutoff near the end. The long plateau in the middle indicates a clear lack of medium-sized quakes for case III. The distribution of cluster size grows fairly extreme, especially as we go from case III to IV.

In order to highlight the effect of large clusters, we calculate the  $n$ -th moment of  $S$ ,  $\langle S^n \rangle$ , and plot the result against  $\dot{\gamma}_{inst}$  in Fig. 7(b). For  $n = 1$ ,  $\langle S \rangle$  only shows a weak dependence on  $\dot{\gamma}_{inst}$  due to the fact that more than 90% of clusters are of size 10 or smaller in all cases. Higher-order moments with  $n = 2$  and 4 result in a distinct peak at the middle shear rates.



**FIG. 6** (a) Distribution of cluster size in time for the four signature cases. Clusters are plotted as circles with area proportional to their sizes,  $S$ . (b~d) 3D reconstructed snapshots of the system, taken at specific moments marked as vertical dashed lines in (a). Two instants  $t_1$  and  $t_2$  are also marked for their reference in the next subsection. Only mobile particles are shown for clarity. Clusters are colored according to its size.



**FIG. 7** (a) Cumulative count of clusters with size  $S$  equal or larger than the number on the horizontal axis, for each of the four signature cases. (b) The mean value  $\langle S^n \rangle^{1/n}$  with  $n = 1, 2, 4$  plotted against  $\dot{\gamma}_{inst}$ , for all cases. The roman numerals mark the four signature cases.

### C. Substructure within a large cluster

The preceding analyses are all based on  $|\delta\vec{r}|$ , leaving the direction of motion unattended. For instance, in Fig.6, the two instants labelled as  $t_1$  and  $t_2$  (in case III, panel (a)) both contribute to a large mobile cluster shown as in its panel (d). But this does not suggest that the entire cluster of particles are moving toward the same direction. To better understand the movements of these particles within a cluster, in this subsection we define  $\delta r_\phi \equiv \delta\vec{r} \cdot \hat{\phi}$  and recover the information of direction.

In Fig.8, the values of  $\delta r_\phi$  for all particles at  $t_1$  and  $t_2$  of case III are color-coded, both from two complimentary angles of view. Panel (a) reveals that most of the particles in the upper half of the cluster move along the direction of the base flow  $\hat{\phi}$  upon the quaking event at  $t_1$ . On the other hand, panel (b) shows that, in the quaking event at  $t_2$ , particles in the lower part of the cluster mostly move against the direction of  $\hat{\phi}$ . This reveals that there are substructures within the mobile cluster that we define in the preceding subsection, awaiting further studies in the future.

In Fig.9, we visualize the distribution of the values of  $\delta r_\phi$  for all particles and for all four signature cases. This is done by color-coding small dots representing each particle according to the value of  $\delta r_\phi$  and spreading them along the z-direction at every instant. Simultaneously, we display the time sequence of normal stress for each case. We see that all those heavily colored instants correspond to significant quaking events. However, not every quaking event find its counterpart in the response of  $\delta r_\phi$ . This is because our current imaging analysis is limited to just half of the cell, therefore some of the localized quaking events that reside in the other half of the cell cannot be captured by the response of  $\delta\vec{r}$ . We are still working on improving the optics to resolve such issue.

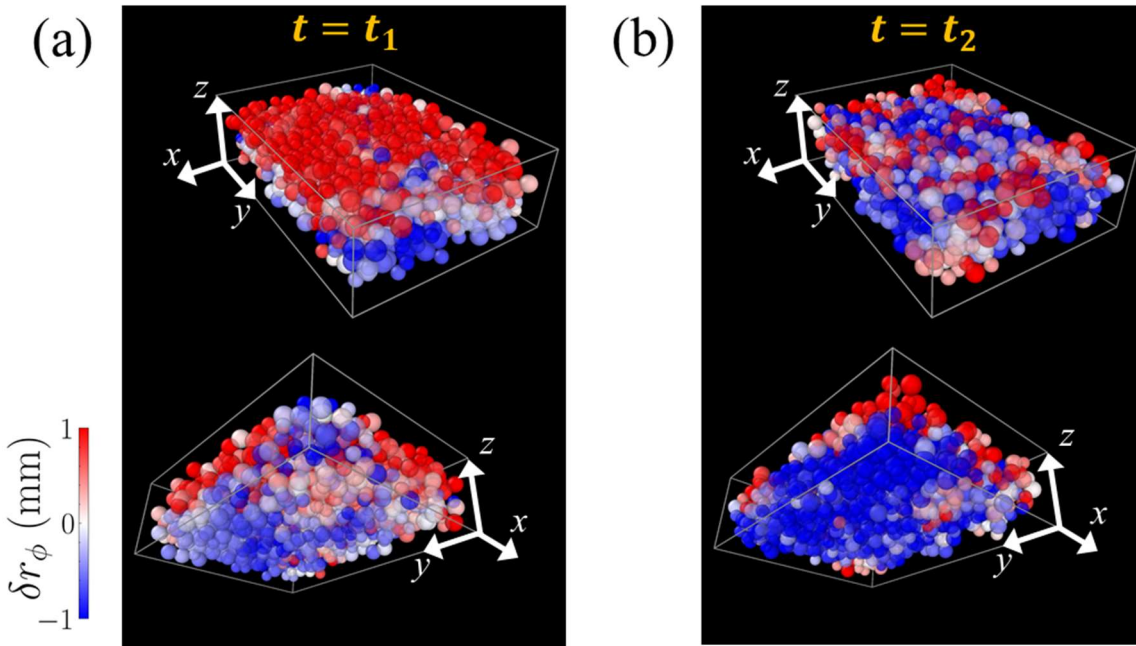


**FIG. 8** Perspective drawings for two quaking events at (a)  $t = t_1$  and (b)  $t = t_2$  in case III, as indicated in Fig.6a (and Fig.9 as well). Particles are color-coded by the value of  $\delta r_\phi$  defined in the main text. For clarity, both cases are captured from two complimentary angles of view.

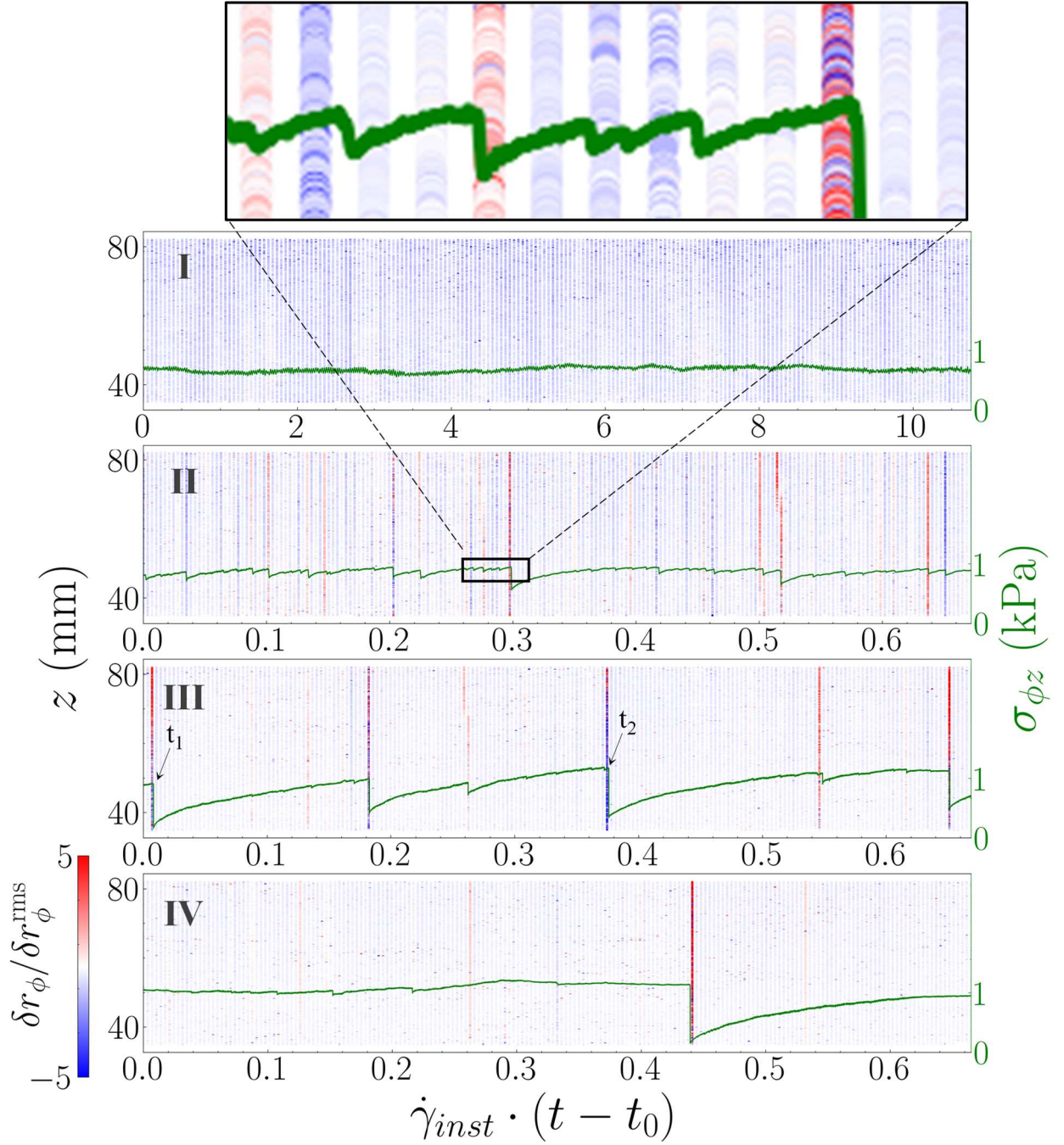


**FIG. 9** Distribution of the values of  $\delta r_\phi$  of every particle, spread out along their  $z$ -positions (as shown by the inset on top) at every instant, overlaid by signals of the instantaneous shear stress  $\sigma_{\phi z}$  (in green, with its axis on the right). Each particle is represented by a small dot that is color-coded by the value of  $\delta r_\phi$  normalized by its root-mean-squared average  $\delta r_\phi^{rms}$  over all particles at all times for each case. The two instants  $t_1$  and  $t_2$  referred in Fig.8 are also indicated.

#### IV. DISCUSSION --- Consistency with our previous work

In this section, we compare the transition identified by the present study to that reported in Ref. [17]. One common observable in the two studies is the shear stress, and the quaking transition can be described by monitoring the large drop (LD) count, defined as the number of drops in shear stress with their magnitude larger than the long-time RMS fluctuation. Fig. 10(a) displays the glaring discrepancy in LD count per strain<sup>2</sup> versus shear rate  $\dot{\gamma}$  for the two studies, implying that the imposed shear rate is not the sole factor in this transition.

To better understand the underlying the transition, we revisit the mechanism proposed in Ref. [17] that emphasizes the role of particle friction and the speed-dependent lubrication. In an independent experiment [23], we have performed tribology measurements between contacting PDMS particles immersed in glycerol solution to mimic the conditions of our granular system, and found that the inter-particle friction decreases drastically once the sliding speed goes beyond a certain threshold,  $V_c$ , that is material dependent. This can be understood as a transition from the regime of solid-solid contact to that of mixed lubrication, commonly understood as part of the Stribeck curve that has been well established in tribology [22,23]. In our follow-up study [24], we have introduced the dimensionless shear rate  $S_\ell \equiv \ell\dot{\gamma}/V_c$ , which compares the generic relative speed between particles of characteristic size  $\ell$  in a uniform shear flow at rate  $\dot{\gamma}$ , to the threshold speed  $V_c$  between contacting particles. Given the binary mixture of 9 mm and 12 mm particles being used in the current study, we set  $\ell = 10$  mm as the characteristic size in calculating the dimensionless shear rate  $S_\ell$ . (In our previous study, we use monodisperse particles so that  $\ell = d = 9$  mm.) Also by independent experiments (see Supplemental Materials), we have found that the threshold speed  $V_c$  in our current system is around 0.2 mm/s, that is substantially lower than the 5 mm/s in Ref. [17].

In Fig. 10(b), we re-plot the LD count as a function of  $S_\ell$  instead of the physical shear rate, for both the previous and the current work. The result shows a reasonably good collapse of the two curves obtained from two experiments using different geometries.

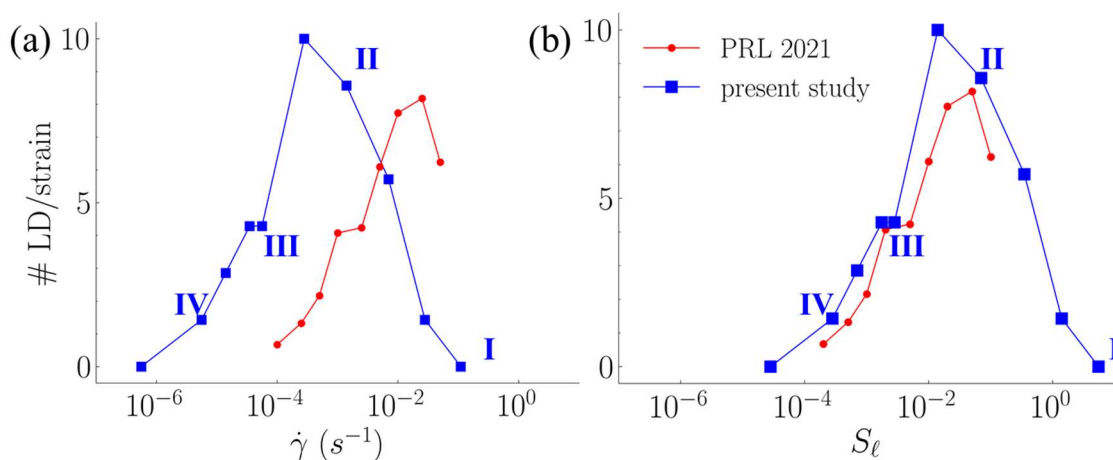


**FIG. 10** Counts of large stress drops (LD) per unit strain plotted as a function of (a) the physical shear rate  $\dot{\gamma}$  and (b) the dimensionless shear rate  $S_\ell$  for data from two different systems: Our previous work published in PRL 2021 [17] and the present study in CSC setup, respectively. Roman numerals mark the four signature cases in our present study.

<sup>2</sup> For the present study, we use the effective shear strain defined in Section II.

## V. SUMMARY

We have prototyped an experimental system in which a continuous circular shearing is imposed to soft granular particles that are tightly packed at a fixed volume. The system allows us to monitor the fluctuation of shear stress and to track the motion of the internal particles. By monitoring the sudden drops of stress, which we call quaking events, and how their occurrence changes with the shear rate, we confirm that the phenomena are consistent with our prior findings as a friction-induced transition, and that the previously proposed dimensionless shear rate ( $S_\ell$ ) incorporates the tribology (the speed dependence of friction) involved and is indeed a good parameter to characterize such transition.

To understand how internal particles move and contribute to the quaking, we compute the fluctuating displacement  $\delta\vec{r}$ , in which the contribution from the base flow imposed by the driving mechanism is removed. We find that

1. The snapshots of  $|\delta\vec{r}|$  reveal the trend that, at high driving rates ( $S_\ell > 1$ ), the particles flow smoothly and the movements exhibits no significant fluctuations over time. At slower driving rates, the distribution of  $|\delta\vec{r}|$  shows a bias toward small displacements, with scarce but very large displacements upon large quaking events. However, as driving rate keeps decreasing ( $S_\ell \sim 10^{-4}$ ), the quaking behavior becomes so extreme that only one large event occurs within our observation window (with an effective strain  $\sim 0.7$ ). Further decrease of the driving rate renders the quaking practically undetectable.
2. By adopting only the particles with the top 5% of  $|\delta\vec{r}|$  and connecting the nearest neighbors, we define clusters of significant displacement and their size  $S$ . The distribution of  $S$  further supports the trend described above. The non-monotonic change of the mean size  $\langle S^n \rangle^{1/n}$  with the driving rate also reflects the trend of growing cluster size with decreasing occurrence of large clusters as the shear rate goes down.
3. By projecting  $\delta\vec{r}$  onto the direction of the base flow ( $\hat{\phi}$ ), substructures in a large cluster reflect localized but somewhat collective movements, awaiting further studies.

The current study is limited to just one packing fraction (0.59). With ongoing improvements to the system reported here, we anticipate to explore the behaviors at variable packing fractions and report the results in future works.

## References

- [1] J. J. Roering, J. W. Kirchner, L. S. Sklar, and W. E. Dietrich, Hillslope evolution by nonlinear creep and landsliding: An experimental study, *Geology* **29**, 143 (2001).
- [2] T. S. Komatsu, S. Inagaki, N. Nakagawa, and S. Nasuno, Creep Motion in a Granular Pile Exhibiting Steady Surface Flow, *Phys. Rev. Lett.* **86**, 1757 (2001).
- [3] N. S. Deshpande, D. J. Furbish, P. E. Arratia, and D. J. Jerolmack, The perpetual fragility of creeping hillslopes, *Nat. Commun.* **12**, 3909 (2021).
- [4] K. E. Daniels and N. W. Hayman, Force chains in seismogenic faults visualized with photoelastic granular shear experiments, *J. Geophys. Res. Solid Earth* **113**, (2008).
- [5] M. Bretz, R. Zaretski, S. B. Field, N. Mitarai, and F. Nori, Broad distribution of stick-slip events in Slowly Sheared Granular Media: Table-top production of a Gutenberg-Richter-like distribution, *Europhys. Lett.* **74**, 1116 (2006).
- [6] D. A. Geller, R. E. Ecke, K. A. Dahmen, and S. Backhaus, Stick-slip behavior in a continuum-granular experiment, *Phys. Rev. E* **92**, 060201 (2015).
- [7] A. S. Argon and H. Y. Kuo, Plastic flow in a disordered bubble raft (an analog of a metallic glass), *Mater. Sci. Eng.* **39**, 101 (1979).
- [8] A. S. Argon and L. T. Shi, Development of visco-plastic deformation in metallic glasses, *Acta Metall.* **31**, 499 (1983).
- [9] M. L. Falk and J. S. Langer, Dynamics of viscoplastic deformation in amorphous solids, *Phys. Rev. E* **57**, 7192 (1998).
- [10] A. Nicolas, E. E. Ferrero, K. Martens, and J.-L. Barrat, Deformation and flow of amorphous solids: Insights from elastoplastic models, *Rev. Mod. Phys.* **90**, 045006 (2018).
- [11] É. Guazzelli and O. Pouliquen, Rheology of dense granular suspensions, *J. Fluid Mech.* **852**, P1 (2018).
- [12] P. Schall, D. A. Weitz, and F. Spaepen, Structural Rearrangements That Govern Flow in Colloidal Glasses, *Science* **318**, 1895 (2007).
- [13] A. Amon, V. B. Nguyen, A. Bruand, J. Crassous, and E. Clément, Hot Spots in an Athermal System, *Phys. Rev. Lett.* **108**, 135502 (2012).
- [14] N. Fernandez, R. Mani, D. Rinaldi, D. Kadau, M. Mosquet, H. Lombois-Burger, J. Cayer-Barrioz, H. J. Herrmann, N. D. Spencer, and L. Isa, Microscopic Mechanism for Shear Thickening of Non-Brownian Suspensions, *Phys. Rev. Lett.* **111**, 108301 (2013).
- [15] N. Y. C. Lin, C. Ness, M. E. Cates, J. Sun, and I. Cohen, Tunable shear thickening in suspensions, *Proc. Natl. Acad. Sci.* **113**, 10774 (2016).
- [16] M. Nabizadeh, A. Singh, and S. Jamali, Structure and Dynamics of Force Clusters and Networks in Shear Thickening Suspensions, *Phys. Rev. Lett.* **129**, 068001 (2022).
- [17] J.-C. (JC) Tsai, G.-H. Huang, and C.-E. Tsai, Signature of Transition between Granular Solid and Fluid: Rate-Dependent Stick Slips in Steady Shearing, *Phys. Rev. Lett.* **126**, 128001 (2021).
- [18] B. Miller, C. O'Hern, and R. P. Behringer, Stress Fluctuations for Continuously Sheared Granular Materials, *Phys. Rev. Lett.* **77**, 3110 (1996).
- [19] D. V. Denisov, K. A. Lörincz, J. T. Uhl, K. A. Dahmen, and P. Schall, Universality of slip avalanches in flowing granular matter, *Nat. Commun.* **7**, 1 (2016).
- [20] A. Lemaître and C. Caroli, Rate-Dependent Avalanche Size in Athermally Sheared Amorphous

Solids, Phys. Rev. Lett. **103**, 065501 (2009).

[21] A. Abed Zadeh, J. Barés, and R. P. Behringer, Crackling to periodic dynamics in granular media, Phys. Rev. E **99**, 040901 (2019).

[22] J. H. H. Bongaerts, K. Fourtouni, and J. R. Stokes, Soft-tribology: Lubrication in a compliant PDMS–PDMS contact, Tribol. Int. **40**, 1531 (2007).

[23] C.-E. Tsai and J.-C. (JC) Tsai, Dynamical force measurements for contacting soft surfaces upon steady sliding: Fixed-depth tribology, Phys. Rev. E **109**, 064802 (2024).

[24] C.-E. Tsai, W.-C. Li, H.-C. Fan-Chiang, P.-Y. Hsiao, and J.-C. Tsai, Two types of quaking and shear unjamming: Case diagram for soft granular particles in quasistatic shear, Phys. Rev. Res. **6**, 023065 (2024).

[25] J. Barés, D. Wang, D. Wang, T. Bertrand, C. S. O’Hern, and R. P. Behringer, Local and global avalanches in a two-dimensional sheared granular medium, Phys. Rev. E **96**, 052902 (2017).

[26] J. A. Dijksman, F. Rietz, K. A. Lőrincz, M. van Hecke, and W. Losert, Invited Article: Refractive index matched scanning of dense granular materials, Rev. Sci. Instrum. **83**, 011301 (2012).

[27] J.-C. Tsai, G. A. Voth, and J. P. Gollub, Internal Granular Dynamics, Shear-Induced Crystallization, and Compaction Steps, Phys. Rev. Lett. **91**, 064301 (2003).

[28] C.-F. Zhao, G. Pinzón, M. Wiebicke, E. Andò, N. P. Kruyt, and G. Viggiani, Evolution of fabric anisotropy of granular soils: x-ray tomography measurements and theoretical modelling, Comput. Geotech. **133**, 104046 (2021).

[29] Y. Xing, J. Zheng, J. Li, Y. Cao, W. Pan, J. Zhang, and Y. Wang, X-Ray Tomography Investigation of Cyclically Sheared Granular Materials, Phys. Rev. Lett. **126**, 048002 (2021).

[30] Y. Cao et al., Structural and topological nature of plasticity in sheared granular materials, Nat. Commun. **9**, 2911 (2018).

[31] A. Penn, T. Tsuji, D. O. Brunner, C. M. Boyce, K. P. Pruessmann, and C. R. Müller, Real-time probing of granular dynamics with magnetic resonance, Sci. Adv. **3**, e1701879 (2017).

[32] Q. Guo, Y. Zhang, A. Padash, K. Xi, T. M. Kovar, and C. M. Boyce, Dynamically structured bubbling in vibrated gas-fluidized granular materials, Proc. Natl. Acad. Sci. **118**, e2108647118 (2021).

[33] D. B. Allan, T. Caswell, N. C. Keim, C. M. van der Wel, and R. W. Verweij, soft-matter/trackpy: v0.6.2, (2024).

[34] J. C. Crocker and D. G. Grier, Methods of Digital Video Microscopy for Colloidal Studies, J. Colloid Interface Sci. **179**, 298 (1996).

[35] A. Stukowski, Visualization and analysis of atomistic simulation data with OVITO—the Open Visualization Tool, Model. Simul. Mater. Sci. Eng. **18**, 015012 (2009).

[36] OVITO — *Scientific Data Visualization and Analysis Software*, <https://www.ovito.org>.

[37] H. Imai, M. Iri, and K. Murota, Voronoi Diagram in the Laguerre Geometry and Its Applications, SIAM J. Comput. **14**, 93 (1985).